

## Original article

# Modelling spontaneous droplet transport in deformable divergent channels

Dongsheng Chen<sup>1</sup>, Haiyi Zhong<sup>1</sup>, Zhongzheng Wang<sup>2</sup>, Si Suo<sup>3</sup>, Deheng Wei<sup>1,4</sup>, Yixiang Gan<sup>1</sup>✉\*

<sup>1</sup>School of Civil Engineering, The University of Sydney, NSW 2006, Australia

<sup>2</sup>School of Mechanical, Medical and Process Engineering, Faculty of Engineering, Queensland University of Technology, QLD 4001, Australia

<sup>3</sup>Department of Civil and Environmental Engineering, Imperial Collage London, London, SW7 2AZ, United Kingdom

<sup>4</sup>State Key Laboratory of Intelligent Deep Metal Mining and Equipment, School of Resources and Civil Engineering, Northeastern University, Shenyang 110819, P. R. China

### Keywords:

Spontaneous droplet transport  
moving contact line  
fluid-solid interaction  
contact angle hysteresis

### Cited as:

Chen, D., Zhong, H., Wang, Z., Suo, S., Wei, D., Gan, Y. Modelling spontaneous droplet transport in deformable divergent channels. *Capillarity*, 2025, 15(1): 4-11. <https://doi.org/10.46690/capi.2025.04.02>

### Abstract:

Spontaneous droplet movement has gained increased interest in many applications, including microfluidics and microfabrication. This study focuses on the numerical investigation of driving mechanisms of spontaneous droplet motion. The numerical model using the phase-field method was validated by available experimental data. In this study, a heterogeneous wettability condition is implemented to reproduce contact angle hysteresis for the accurate prediction of spontaneous droplet dynamics. Through analysing the capillary pressure within the droplet, the driving mechanism is identified as being governed by the pressure difference between the two interfaces which depends on channel configuration, wettability, and contact angle hysteresis. The impact of channel deformability was further studied, revealing that channel deformability leads to significant changes in velocity or even reversed droplet movement direction. This study provides a novel numerical framework for controllable spontaneous droplet movement in flexible channels.

## 1. Introduction

Controlled droplet movement has attracted significant attention in many technological applications, e.g., microfluidics (Squires et al., 2005), hairy coating (Wang et al., 2015), microchemical reactions (Li et al., 2020a, 2020b), and textile products (Wang et al., 2020; Guan et al., 2021). Bio-inspired droplet transports have gained increased interest, particularly the spontaneous droplet transport, including the self-removal of water from legs of water-striders (Wang et al., 2015), gravity-opposing feeding process of shorebirds facilitated by their beak geometry (Prakash et al., 2008), and transport of liquid on the leaves and shoots of some plants by surface

structures (Feng et al., 2021; Yang et al., 2024). A spontaneous movement requires no external energy input and offers potential for a wide range of technological applications.

These capillary-driven droplet movements can be categorised into two types depending on the deformability of the solid structure. For a non-deformable structure, or fixed solid boundary, spontaneous liquid movement has been achieved in wedge-shaped (Reyssat, 2014) or on conical (Lv et al., 2014) geometry. The second scenario is where the solid structure may deform under the capillary interaction of the droplet, which subsequently facilitates the droplet motion. Examples include *durotaxis* where the deformation is attributed to stiffness gra-

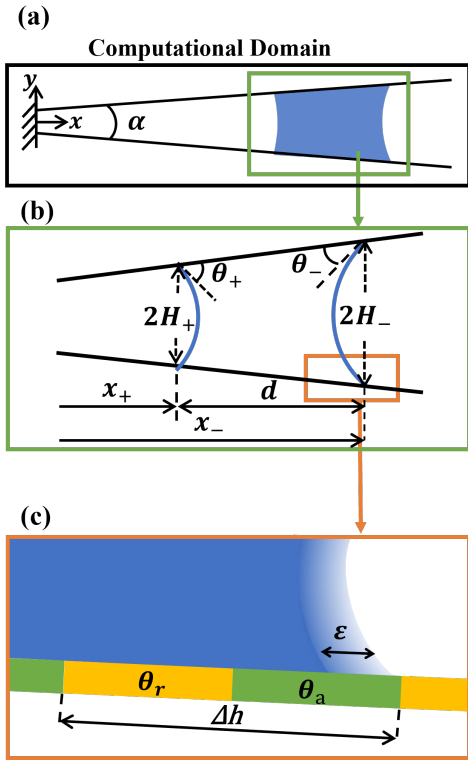


**Fig. 1.** Droplet model setup: (a) The fluid (blue) is placed between the non-parallel channels with an opening angle  $\alpha$ , (b) magnified schematic showing the dimension of the droplet between the channels, and (c) details of phase-field model at liquid-gas contact line and applied contact angle waveform function on the wall boundary. The alternating yellow and green strips on the solid surface indicate the region with receding and advancing contact angles, respectively. The interface thickness for the phase-field model is indicated by  $\epsilon$ .

dients (Style et al., 2013), *tensotaxis* during which the deformation is induced by strain gradients (Bueno et al., 2017), and *bendotaxis* where deformable parallel channels drive the droplet to the free end (Bradley et al., 2019). Recently, Zhong et al. (2025) experimentally investigated the spontaneous droplet movement involving solid-liquid interaction. Extending from bendotaxis, the droplet movement between a pair of nonparallel flexible channels was examined, highlighting that the droplet movement direction can be controlled by carefully tuning the channel inclination angle, contact angle, and bendability.

One of the remaining challenges is to understand the role of Contact Angle Hysteresis (CAH) during spontaneous droplet movement (Bradley et al., 2019; Zhong et al., 2025). CAH is the difference in the contact angles between the advancing (liquid-invading-vapor,  $\theta_a$ ) and the receding (vapor-invading-liquid,  $\theta_r$ ) fronts of a moving droplet. It originates from surface chemical heterogeneity, roughness, deformation, and adaptation of the solid surface to a fluid during their interaction, etc (Butt et al., 2022), and therefore CAH cannot be avoided in most situations (McCarthy et al., 2019). For

theoretical works, CAH is usually neglected for simplicity, typically leading to the overestimation of the droplet motion (Lv et al., 2014). As CAH is an inherent physical phenomenon, it is essential to incorporate CAH to precisely predict the droplet transport behaviour (Shi et al., 2018).

Recently, many researchers have attempted to reproduce CAH by investigating the effects of surface heterogeneity on droplet dynamics with acceptable accuracy (Snoeijer et al., 2013). Experimental and numerical works have shown that chemically patterned surfaces can successfully produce desired CAH effects (Kusumaatmaja and Yeomans, 2007; Varagnolo et al., 2014). Luo et al. (2017) modelled topologically rough surfaces, used to investigate CAH by simulating droplet spreading, verified by numerical simulations. Inspired by these prior approaches, this study adopts a similar static heterogeneous waveform boundary condition as it is computationally efficient while sufficiently captures CAH effects.

This study investigates the effects of CAH and solid deformability on spontaneous droplet transport between a pair of deformable nonparallel channels. To fully understand the coupled effects of deformability and CAH, a numerical model implementing the phase-field method (Jacqmin, 1999) with a contact angle boundary condition generated using waveform function was developed (Kusumaatmaja and Yeomans, 2007; Varagnolo et al., 2014). The model was firstly calibrated and validated against the experimental work by Prakash et al. (2008) and then applied to investigate the effects of solid deformability. This study provides a numerical framework for further understanding of influences of channel configuration, CAH, and channel flexibility on spontaneous droplet motion, with potential applications to microfluidics and biomedical devices.

## 2. Methodology

A 2D numerical model was developed in COMSOL Multiphysics® 6.1. The model closely replicates the experimental setup described in Prakash et al. (2008), as illustrated in Fig. 1. A rectangular computational domain contains a non-parallel channel with an opening angle  $\alpha$ , in which a droplet is placed, as shown in Fig. 1(a). The channel consists of a liquid droplet of length  $d$  (Fig. 1(b)) placed between two solid substrates that are symmetrical about the horizontal axis. The origin,  $(x,y) = (0,0)$ , is defined on the symmetry axis, at the narrow and fixed end. The substrates are linear elastic materials and with the length,  $l$ , and the thickness,  $b$ , is purely elastic denoted by Young's modulus,  $E$ , and Poisson's ratio  $\nu$ . Given the symmetrical geometric dimension of the liquid, the gravitational force is ignored.

### 2.1 Governing equations

The phase-field method is adopted to capture the dynamics of droplet movement (Jacqmin, 1999; Yue et al., 2004; Suo et al., 2024), which couples the Stokes equations with the Cahn-Hilliard equations, establishing the relationship between the

pressure  $p$ , velocity  $v$ , and the phase-field variable  $\phi \in [-1, 1]$  representing the fluid fraction, where  $\phi = 1$  and  $-1$  are for the pure liquid and the gas phases, respectively. The gas-liquid interface is at  $\phi = 0$ . The mass conservation, scalar transport, and momentum balance are formulated in order:

$$\nabla \cdot v = 0 \quad (1)$$

$$\frac{\partial \phi}{\partial t} + v \cdot \nabla \phi = M \nabla^2 G \quad (2)$$

$$-\nabla p + \mu(\phi) \nabla^2 v + G \nabla \phi = 0 \quad (3)$$

where  $t$  is time,  $M$  is the mobility parameter,  $G \nabla \phi$  the interfacial force,  $\mu$  the viscosity of the mixed fluid, and  $G$  the bulk chemical potential:

$$G = \omega [-\nabla^2 \phi + (\phi^2 - 1) \phi / \varepsilon^2] \quad (4)$$

where  $\varepsilon$  characterizes the interface thickness (Fig. 1(c)), while  $\omega$  represents the mixing energy density, which is linked to the surface tension through the relation  $\sigma = 2\sqrt{2}\omega/(3\varepsilon)$ . It is assumed that  $\mu(\phi)$  conforms to an arithmetic mean of the liquid ( $\mu_l$ ) and gas ( $\mu_g$ ) viscosities:

$$\mu(\phi) = \frac{1+\phi}{2}\mu_l + \frac{1-\phi}{2}\mu_g \quad (5)$$

Such a definition gives a smooth viscosity transition between the two phases. The present study adopts the steady-state Navier-Stokes equations without the convection term, consistent with the phase-field-based modelling framework described by Wang et al. (2019). This simplification is particularly appropriate for interfacial two-phase flows under low Reynolds number conditions, where viscous and capillary effects dominate, and inertia is negligible. More details of the phase field model can be referred to (Jacqmin, 1999).

Macroscopic length scales in the Cahn-Hilliard model play a crucial role in capillary-dominated flows, and it is important to select appropriate model parameters (Suo et al., 2024). Particularly, the assumed interface thickness  $\varepsilon$  is an influencing factor of the bulk chemical potential  $G$ . The interfacial diffusion length  $l_d$  of  $G$  was introduced by Yue et al. (2004) and defined as  $l_d = \sqrt{M\mu_e}$ , where  $\mu_e$  is the effective viscosity of the two phases, defined as  $\mu_e = \sqrt{\mu_g\mu_l}$ , and the artificial parameter  $M$  serves as the diffusion coefficient. To select appropriate values for  $M$  and  $l_d$ , the slip length  $l_s$  derived from microscopic contact line motion provides a useful framework for modelling macroscopic hydrodynamics away from the contact line (Cox, 1986; Eggers, 2005). Jacqmin et al. (2000) first proposed the relation between  $l_d$  and  $l_s$ , which was later refined by Yue and Feng (2011). They suggested the criterion  $l_s = 2.5l_d$ , which was further validated by Gao et al. (2019).

Liquid-vapour interfaces are generally at the nanoscale, which makes smaller interface thickness ( $\varepsilon$ ) values preferable, as they can more accurately represent physical phenomena by reducing artificial energy dissipation and better approximating a sharp interface. However, decreasing the interface thickness requires finer mesh and smaller time steps to maintain numerical stability, significantly increasing the computational

cost. Hence, the selection of  $\varepsilon$ , characterised by the Cahn number  $C_n = \varepsilon/H$  ( $H$  is the average channel height), should balance accuracy and computational efficiency. To ensure reliable results,  $\varepsilon$  should be chosen such that the numerical solution reaches the sharp-interface limit, beyond which further reduction has a negligible effect on the results, indicating the independence on  $C_n$  (Suo et al., 2024). Previous studies have suggested several selection criteria. Gao et al. (2019) and Peng et al. (2021) suggested that  $C_n \leq 0.025$  ensures numerical convergence, while Yue et al. (2010) recommended that  $C_n \leq 4S$ , where  $S = l_d/H$  is the relative slip length. For problems with a characteristic capillary length on the order of 1mm, the corresponding  $C_n$  and  $S$  are on the order of  $10^{-5}$ , which poses computational challenge for the phase field method (Suo et al., 2024). In this study,  $C_n = 0.01$  and  $S = 0.004$  is adopted (Suo et al., 2024), resulting in  $l_s = 0.01H$ , which is appropriate for capturing geometric effects on interfacial dynamics with reasonable computational effort. Therefore, in this study,  $\varepsilon = 1.6 \times 10^{-5}$  m.

## 2.2 Meshing and boundary conditions

Triangular meshing is applied to the entire fluid domain, while a quadratic mesh is used for the solid substrates. Additionally, to avoid meshing issues that arise from sharp corners or severe mesh distortion, geometric smoothing is applied in the fluid domain between the solid substrates. The model employs linear shape functions for fluid flow and quadratic shape functions for solid mechanics problems, ensuring accuracy in fluid-structure interactions. Outlet boundary conditions were applied to the left and right boundaries, while wall boundary conditions were applied to the top and the bottom boundaries. Fixed boundary conditions are assigned to the ends of substrates at the narrow opening, illustrated in Fig. 1(a).

## 2.3 CAH

To consider CAH effects in this numerical study, a spatially heterogeneous wetting condition was implemented using a square waveform function along the solid substrate to define the local contact angle  $\theta(x)$ . Each period contains an advancing and receding contact angle segment, as shown in Fig. 1(c), representing microscale surface heterogeneity. This method has been widely used (Kusumaatmaja and Yeomans, 2007; Varagnolo et al., 2014) for its efficiency in replicating CAH effects in phase-field simulations. The variation of the contact angle along the substrate can be expressed as:

$$\theta(x) = \begin{cases} \theta_a = \theta_e + \Delta\theta, & \text{if } x \bmod \Delta h < \frac{\Delta h}{2} \\ \theta_r = \theta_e - \Delta\theta, & \text{if } x \bmod \Delta h \geq \frac{\Delta h}{2} \end{cases} \quad (6)$$

where  $\Delta\theta$  represents the magnitude of the CAH, and  $\theta_e$  corresponds to the equilibrium contact angle.

It should be noted that the chosen wavelength can affect the droplet motion and may lead to undesired nonphysical behaviours if not properly defined. To avoid artificial pinning, the size of the microscale surface heterogeneity should be much smaller than the radius of curvature of the contact line

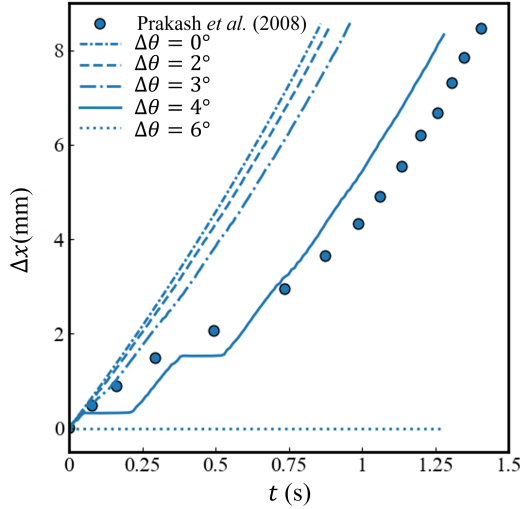


**Fig. 2.** Droplet motion for calibrating CAH value, with  $25^\circ$  as the equilibrium contact angle and hysteresis values  $\theta_h$  of  $0^\circ$ ,  $2^\circ$ ,  $3^\circ$ ,  $4^\circ$  and  $6^\circ$ , and a channel opening  $\alpha$  of  $1.9^\circ$  (i.e.,  $\alpha_1$  from Prakash et al. (2008)).

(Butt et al., 2022), and larger than the interfacial thickness to provide prescribed CAH. Based on this assumption, a criterion for implementing the CAH boundary condition was proposed as such:

$$d \gg \Delta h \gg \varepsilon \quad (7)$$

where  $d$  is the initial droplet length, representing the characteristic length scale of the droplet. This criterion helps reduce numerical errors in the boundary condition equations by averaging the influence of local heterogeneity introduced through the waveform function.

#### 2.4 Model parameters and calibration

The problem setup is based on the experiments conducted by Prakash et al. (2008), the results of which are also used for model parameter calibration and validation. Several parameters were adopted directly from the original experimental specifications as follows. The solid substrates have a length  $l$  of 20 mm, thickness  $b$  of 0.15 mm. The working fluid is silicone oil with dynamic viscosity  $\eta = 0.01$  Pa s, the ambient fluid is air with the dynamic viscosity  $\eta = 1.81 \times 10^{-5}$  Pa s, and surface tension coefficient  $\gamma$  of the interface is 0.02 N/m (silicone oil in air at ambient conditions). The configuration featured three predefined values for the opening angle  $\alpha$ ,  $\alpha_1 = 1.9$ ,  $\alpha_2 = 2.8$ ,  $\alpha_3 = 4.2$ . The droplet volume based on their results was approximately  $1 \mu\text{L}$  and the equilibrium contact angle was measured to be around  $25^\circ$ . Since the CAH was not explicitly reported, the following section presents a calibration process to acquire a reasonable  $\Delta\theta$ .

Simulations were conducted to determine the most suitable CAH value, in order to recreate the experiment by Prakash et al. (2008) in simulation. Model setup remains identical to the experiment except for a changing  $\Delta\theta$  value, increasing from  $0^\circ$  to  $6^\circ$ . The implemented CAH is validated by simulating

a droplet on a tilting plane. Fig. 2 shows the displacement of the droplet centre ( $\Delta x$ ) of the silicone oil droplet with time. The CAH effects have been demonstrated among these cases, showing a decreasing average moving speed with an increasing CAH effect. The case illustrated by solid line  $\Delta\theta = 4^\circ$  in Fig. 2 is best matched with the experimental movement of the droplet. There are two temporary stagnant stages observed in the numerical model, which are also likely in the experiments if the time intervals are sufficiently small in the observation. The average moving speed, i.e., the slope of the droplet displacement curves, is the key factor determining the goodness of predictions. Therefore, a CAH  $\Delta\theta = 4^\circ$  is adopted for all subsequent simulations.

### 3. Results and discussions

#### 3.1 Validation results

Fig. 3 compares the computed results from the calibrated model with the experimental data on the opening angle reported by Prakash et al. (2008). It should be noted that the centre of the droplet is tracked for representing the droplet motion instead of its trailing edge as in the original experiments, since this treatment separates the droplet motion and spreading, in particular for later results on deformable channels. In general, the numerical model using the implemented CAH can well capture the trend of droplet movement over time for three different opening angles. Simulation results and experimental data shows especially good agreement at large opening angle (i.e.,  $\alpha_3$ ), with a R-squared value of 0.93. However, discrepancies are more pronounced in the other two values of  $\alpha$ , with a lowest R-squared value of 0.74 between the computed and experimental results. This can be attributed to two possible reasons: 1) Uncertainty in droplet volume. The droplet volume used in the experimental study is around  $1 \mu\text{L}$ . Achieving precise volume control at this scale is challenging, and even a small volume residual in the micropipette tip can introduce errors. 2) Surface roughness. The experimental study used stainless steel polished with diamond slurry for droplet transport, and the reached surface roughness may still contain uncertainty in CAH in different cases. As the opening angle decreases (i.e., the capillary pressure gradient weakens, to be discussed in the next section), the increased adhesion due to roughness can hinder droplet movement (Imani et al., 2023). Consequently, compared to idealised conditions in simulations, the droplet moves relatively slower in experiments. Overall, numerical simulations present reasonable alignment with the experimental data, proving the capability of predicting the capillary-driven droplet movement accounting for the CAH.

#### 3.2 Effects of opening angle and CAH

As discussed in the calibration and validation sections, the channel opening angle and hysteresis value play important roles in the spontaneous motion of the droplet. To further investigate the underlying mechanism, this section proposed a simplified mathematical model for explanation. The schematic of the system is illustrated in Fig. 1(b). Subscripts “-” and “+” are used to differentiate the left and right gas-liquid interfaces of the droplet at a given time, respectively.  $\theta_i$  is the contact

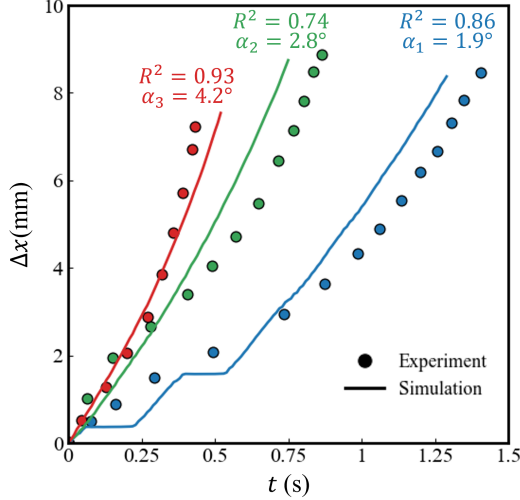


**Fig. 3.** Comparison of experimental and simulation results for different opening angles,  $\alpha_1 = 1.9^\circ$ ,  $\alpha_2 = 2.8^\circ$ ,  $\alpha_3 = 4.2^\circ$ , and the contact angles  $\theta = 25^\circ \pm 4^\circ$ .

angle of the corresponding interface,  $H_i$  is the channel height from  $y = 0$  at interface  $i$ , and  $x_i$  is the  $x$  coordinate.

Here, the capillary pressure contribution is dominated by the out-of-plane curvature, which is much greater than that of the in-plane curvature. Thus, the curved in-plane contact line can be ignored, simplifying the model to this 2D assumption of the  $(x, y)$  plane of the slender channels. The well-known Young-Laplace equation is used to describe the capillary pressure across the air-oil interface. Hence, the capillary pressure  $p_i$  at the two menisci can be written as:

$$p_- = \frac{-\gamma}{H_-} \cos\left(\theta_- - \frac{\alpha}{2}\right) \quad (8)$$

$$p_+ = \frac{-\gamma}{H_+} \cos\left(\theta_+ + \frac{\alpha}{2}\right) \quad (9)$$

where  $H_i$  is calculated using  $H_i = x_i \tan \frac{\alpha}{2}$ . Thus,  $H_+ = H_- + d \cdot \tan \frac{\alpha}{2}$ . The net pressure across the droplet can be expressed as:

$$\Delta p = \gamma \left( \frac{-\cos\left(\theta_- - \frac{\alpha}{2}\right)}{H_-} + \frac{\cos\left(\theta_+ + \frac{\alpha}{2}\right)}{H_- + d \cdot \tan \frac{\alpha}{2}} \right) \quad (10)$$

This equation explains the influence of the opening angle. When  $\alpha$  increases, the channel becomes more diverging. The capillary pressure at the left interface increases due to changes in curvature, whereas for the right interface, capillary pressure decreases. Simultaneously, the difference in the radii of curvature between the two interfaces also increases, further decreasing the driving capillary pressure for the right interface. Consequently, the capillary pressure across the droplet expressed in Eq. (10) shows that as channel opening increases, capillary pressure at the left interface becomes more dominant, which drives the droplet towards the apex.

When assuming that the droplet is in motion towards the narrow end, which is commonly observed in this study,  $\theta_-$  is the advancing contact angle and  $\theta_+$  is the receding contact angle. Incorporating the CAH in the driving mechanism

expression gives:

$$\Delta p = \gamma \left( \frac{-\cos\left(\theta_e + \Delta\theta - \frac{\alpha}{2}\right)}{H_-} + \frac{\cos\left(\theta_e - \Delta\theta + \frac{\alpha}{2}\right)}{H_- + d \cdot \tan \frac{\alpha}{2}} \right) \quad (11)$$

The above equation considers the effect of contact angle  $\theta_e$  and the CAH  $\Delta\theta$  on the curvature of the interfaces. As expressed in Eq. (11), increasing contact angle and the hysteresis effect leads to decreased pressure difference and impeded contact line motion. Heterogeneous surface feature is a major contribution factor to CAH. In this numerical model, the applied heterogeneous boundary condition slows down the contact line motion, simulating such hysteresis effects. The mathematical equation developed here provides analytical insight into the simulation and experimental trends, complementing the quantitative comparison shown in Figs. 2 and 3 and help to reveal the physical mechanism underlying the trends.

### 3.3 Effects of solid deformability

Previous sections primarily focused on investigating droplet motion within fixed channels (i.e.,  $E \rightarrow \text{Infinity}$ ). As demonstrated in recent experiments, structural deformability can introduce additional complexity to droplet dynamics (Zhong et al., 2025). In this study, the material is assumed to be linear elastic and isotropic and is subjected to uniaxial loading, conditions under which Young's modulus reliably characterises its stiffness. Moreover, the substrate is modelled as a cantilever beam deformed by the capillary force, with its bending behaviour governed by  $1/(EI)$  where  $I$  depends on the substrate thickness. In this framework, variations in  $E$  have equivalent effects to changes in substrate thickness on bendability, thereby justifying the use of Young's modulus as an effective descriptor of the solid deformability.

As the Young's modulus of the channels decreases beyond a certain threshold, the capillary force can deform the channel sufficiently such that channel becomes converging or diverging depending on the combination of the wettability condition and channel flexibility. As shown in Fig. 4(a), the free ends initially move toward the centreline, indicating that channel converges and the degree of deformation increases with solid flexibility. Interestingly, the channel exhibits a gradual restoration afterward, except the extremely soft channels (i.e.,  $E = 0.7$  GPa). This is attributed to the deformation induced by the droplet motion, keeping the opening angle in a diverging configuration. In these cases, the pressure gradient as described by Eq. (11) continues to drive the droplet toward the fixed end, as illustrated in Case (ii) in Fig. 4(c). Simultaneously, the force application point shifts toward the fixed end, which shortens the effective lever arm and results in reduced deflection. While for the extremely soft case, the capillary force is strong enough to deform the channels from a diverging shape to a converging shape, as in Case (iii) in Fig. 4(c). Hence, for sufficiently large deformation due to small  $E$ , the free ends become even narrower than the left fixed end, resulting in opposite movement direction for the droplet. Such a phenomenon, where there is an interplay between solid deformation and droplet motion, can be observed in some biological systems. For example,

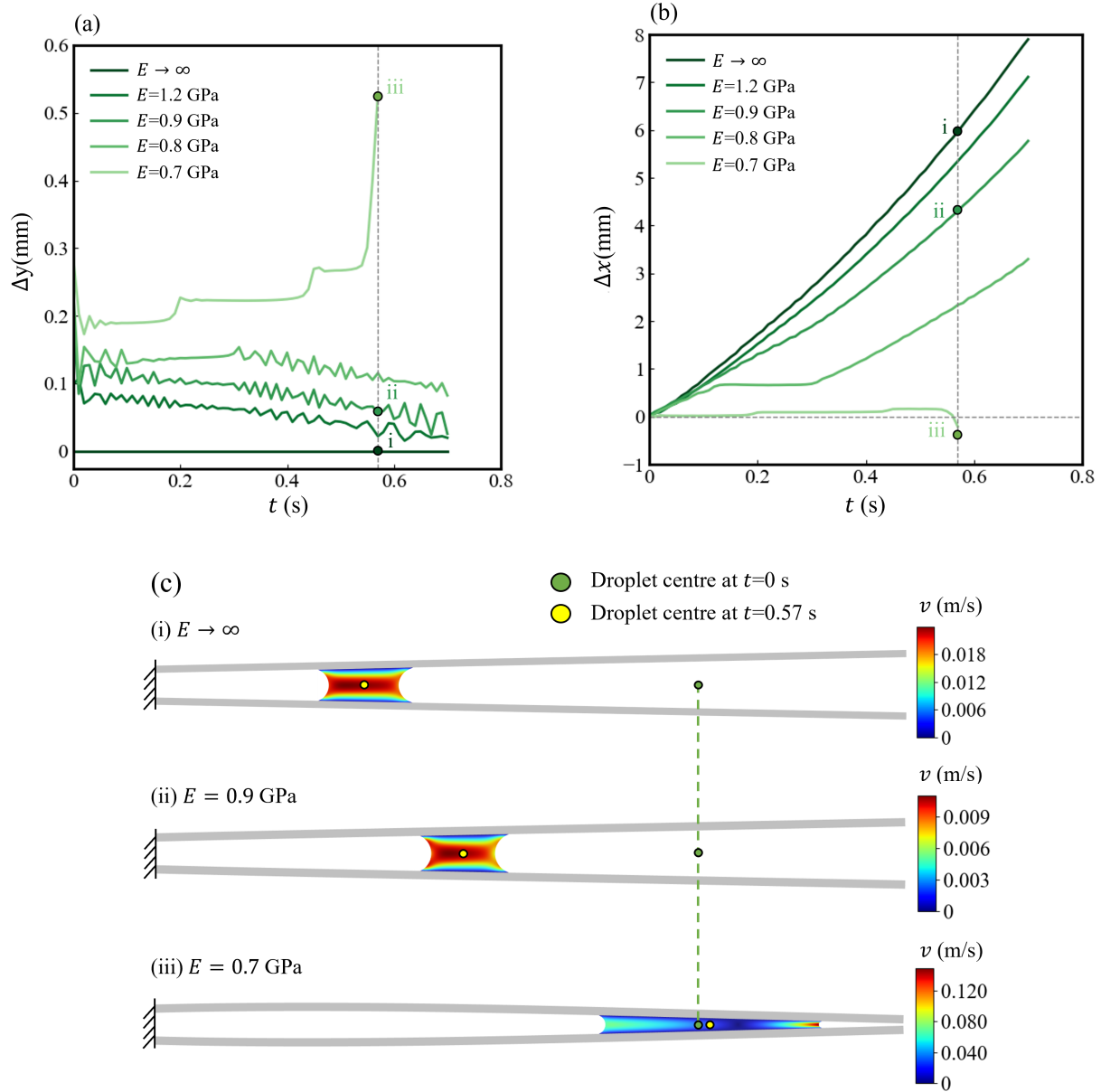


**Fig. 4.** Effect of channel deformability: (a) The free-end vertical displacement of the solid substrate versus time, (b) droplet centre displacement versus time and (c) contour plots of velocity magnitude for Cases (i), (ii) and (iii) shown in (a). (Channels left ends are fixed and right ends are free.)

Wang et al. (2015) observed that in water striders, the setae on the leg are repeatedly tapered by the generation and movement of water droplets.

The channel deformation can further affect the droplet motion, as presented in Fig. 4(b). As the Young's modulus increases except the extremely soft channels (i.e.,  $E = 0.7$  GPa), the droplet motion towards the fixed end is slowed, as shown in Cases (i) and (ii) in Fig. 4(c). This occurs due to the pressure gradient driving the droplet decrease as the channel becomes more converging. This observation aligns with the theoretical model proposed in Section 3.2. A particularly interesting case arises when  $E = 0.7$  GPa. The extremely soft

channels are significantly deformed by the capillary force, eventually shifting the channel from diverging to converging, as shown in Case (iii) in Fig. 4(c). Once the effective opening angle  $\alpha$  becomes negative, the pressure gradient reverses, driving the droplet towards the free ends. These findings demonstrate that by manipulating influencing factors such as structural flexibility (by controlling the material stiffness and plate thickness), the droplet movement can be tuneable, which has also been reported by Zhong et al. (2025).

The investigation in this work is centred on hydrophilic surfaces, as in Prakash et al. (2008). The cases explored in this paper are limited to the given wettability conditions.

Recent experimental work (Zhong et al., 2025) presented a combined effect from the interplay between wettability and deformability conditions. Further studies using this numerical framework can cover a wider range of wettability conditions (e.g., the combination of equivalent and hysteretic contact angles) exploring ranges exceeding experiments, enabling accurate predictions of droplet motion in deformable channels of arbitrary geometry and providing access to the internal dynamics within moving droplets.

#### 4. Conclusions

In this study, a numerical framework for modelling the dynamics of spontaneous droplet motion in flexible channels was implemented. The focus is the interplay between deformable solid substrates and liquid interfaces incorporating the CAH effects. Key findings are as listed:

- 1) The numerical model based on the phase field method for describing the liquid-gas interface and fluid-structure interaction for considering the solid deformation is proposed and shows the capability for solving the class of problems related to capillary interactions in deformable structures.
- 2) A specific boundary condition was developed to consider the CAH. It was validated by comparing with the existing experimental results. A proper consideration of CAH provides reliable numerical predictions, benchmarking to the experimental results. The absence of such consideration can lead to significant error.
- 3) Channel flexibility significantly influences droplet behaviour both in terms of moving velocity and direction. As the flexibility of channel decreases, the channel configuration changes and hence the capillary pressure gradient, as the driving force for the motion. At sufficiently low deformability, the droplet motion can even be reversed in moving direction, thereby enabling the tuneable spontaneous droplet movement.

These findings enhance the understanding of the fluid-solid interactions by incorporating the effects of CAH using a wave-form boundary condition. The results reveal the fundamental mechanisms governing spontaneous droplet transport, particularly highlighting the interplay between structural flexibility, wettability, and channel configuration. By clarifying the role of these factors, this study contributes valuable guidelines for precise control and tuning of droplet motion, with applications in designing the self-cleaning surfaces.

#### Acknowledgements

YG and DW acknowledge the financial supports by Australian Research Council (ARC) under projects of LP200200779, DP230102229 and DE240101106.

#### Conflict of interest

The authors declare no competing interest.

**Open Access** This article is distributed under the terms and conditions of the Creative Commons Attribution (CC BY-NC-ND) license, which permits unrestricted use, distribution, and reproduction in any medium, provided the

original work is properly cited.

#### References

- Bradley, A. T., Box, F., Hewitt, I. J., et al. Wettability-independent droplet transport by bendotaxis. *Physical Review Letters*, 2019, 122(7): 074503.
- Bueno, J., Bazilevs, Y., Juanes, R., et al. Droplet motion driven by tensotaxis. *Extreme Mechanics Letters*, 2017, 13: 10-16.
- Butt, H.-J., Liu, J., Koynov, K., et al. Contact angle hysteresis. *Current Opinion in Colloid & Interface Science*, 2022, 59: 101574.
- Cox, R. G. The dynamics of the spreading of liquids on a solid surface. Part 1. Viscous flow. *Journal of Fluid Mechanics*, 1986, 168: 169-194.
- Eggers, J. Existence of receding and advancing contact lines. *Physics of Fluids*, 2005, 17(8): 082106.
- Feng, S., Zhu, P., Zheng, H., et al. Three-dimensional capillary ratchet-induced liquid directional steering. *Science*, 2021, 373(6561): 1344-1348.
- Gao, P., Liu, A., Feng, J. J., et al. Forced dewetting in a capillary tube. *Journal of Fluid Mechanics*, 2019, 859: 308-320.
- Guan, X., Wang, X., Huang, Y., et al. Smart textiles with janus wetting and wicking properties fabricated by graphene oxide coatings. *Advanced Materials Interfaces*, 2021, 8(2): 2001427.
- Imani, G., Zhang, L., Maweja, J., et al. Effect of roughness on droplet motion in a capillary channel: A numerical study. *Physics of Fluids*, 2023, 35(11):112011.
- Jacqmin, D. Calculation of two-phase navier-stokes flows using phase-field modeling. *Journal of Computational Physics*, 1999, 155(1): 96-127.
- Jacqmin, D. Contact-line dynamics of a diffuse fluid interface. *Journal of Fluid Mechanics*, 2000, 402: 57-88.
- Kusumaatmaja, H., Yeomans, J. M. Modeling contact angle hysteresis on chemically patterned and superhydrophobic surfaces. *Langmuir*, 2007, 23(11): 6019-6032.
- Li, A., Li, H., Li, Z., et al. Programmable droplet manipulation by a magnetic-actuated robot. *Science Advances*, 2020a, 6(7): eaay5808.
- Li, H., Fang, W., Zhao, Z., et al. Droplet precise self-splitting on patterned adhesive surfaces for simultaneous multidetection. *Angewandte Chemie International Edition*, 2020b, 59(26): 10535-10539.
- Luo, L., Wang, X.-P., Cai, X.-C. An efficient finite element method for simulation of droplet spreading on a topologically rough surface. *Journal of Computational Physics*, 2017, 349: 233-252.
- Lv, C., Chen, C., Chuang, Y.-C., et al. Substrate curvature gradient drives rapid droplet motion. *Physical Review Letters*, 2014, 113(2): 026101.
- McCarthy, J., Vella, D., Castrejón-Pita, A. A. Dynamics of droplets on cones: Self-propulsion due to curvature gradients. *Soft Matter*, 2019, 15(48): 9997-10004.
- Peng, X., Wang, X., Du, Z., et al. Phase-field simulations of precursor film in microcapillary imbibition for liquid-

- liquid systems. *International Journal of Multiphase Flow*, 2021, 144: 103789.
- Prakash, M., Quéré, D., Bush, J. W. Surface tension transport of prey by feeding shorebirds: The capillary ratchet. *Science*, 2008, 320(5878): 931-934.
- Reyssat, E. Drops and bubbles in wedges. *Journal of Fluid Mechanics*, 2014, 748: 641-662.
- Shi, Z., Zhang, Y., Liu, M., et al. Dynamic contact angle hysteresis in liquid bridges. *Colloids and Surfaces A: Physicochemical and Engineering Aspects*, 2018, 555: 365-371.
- Snoeijer, J. H., Andreotti, B. Moving contact lines: Scales, regimes, and dynamical transitions. *Annual Review of Fluid Mechanics*, 2013, 45: 269-292.
- Squires, T. M., Quake, S. R. Microfluidics: Fluid physics at the nanoliter scale. *Reviews of Modern Physics*, 2005, 77(3): 977-1026.
- Style, R. W., Che, Y., Park, S. J., et al. Patterning droplets with durotaxis. *Proceedings of the National Academy of Sciences*, 2013, 110(31): 12541-12544.
- Suo, S., O'Kiely, D., Liu, M., et al. Geometry effects on interfacial dynamics of gas-driven drainage in a gradient capillary. *Water Resources Research*, 2024, 60(9): e2023WR036766.
- Varagnolo, S., Schiocchet, V., Ferraro, D., et al. Tuning drop motion by chemical patterning of surfaces. *Langmuir*, 2014, 30(9): 2401-2409.
- Wang, H., Yuan, X., Liang, H., et al. A brief review of the phase-field-based lattice boltzmann method for multiphase flows. *Capillarity*, 2019, 2(3): 32-52.
- Wang, Q., Yao, X., Liu, H., et al. Self-removal of condensed water on the legs of water striders. *Proceedings of the National Academy of Sciences of the United States of America*, 2015, 112(30): 9247-9252.
- Wang, Y., Liang, X., Zhu, H., et al. Reversible water transportation diode: Temperature-adaptive smart janus textile for moisture/thermal management. *Advanced Functional Materials*, 2020, 30(6): 1907851.
- Yang, L., Li, W., Lian, J., et al. Selective directional liquid transport on shoot surfaces of *Crassula muscosa*. *Science*, 2024, 384(6702): 1344-1349.
- Yue, P., Feng, J., Liu, C., et al. A diffuse-interface method of simulating two-phase flows of complex fluids. *Journal of Fluid Mechanics*, 2004, 515: 293-317.
- Yue, P., Feng, J. J. Can diffuse-interface models quantitatively describe moving contact lines? *The European Physical Journal Special Topics*, 2011, 197(1): 37-46.
- Yue, P., Zhou, C., Feng, J. J. Sharp-interface limit of the cahn–hilliard model for moving contact lines. *Journal of Fluid Mechanics*, 2010, 645: 279-294.
- Zhong, H., Wang, Z., Suo, S., et al. Tunable spontaneous droplet motion in flexible channels. *Langmuir*, 2025, 41(11): 7355-7363.